Quantum Electronics **50** (8) 714–719 (2020) ©2020 Kvantovaya Elektronika and IOP Publishing Limited

https://doi.org/10.1070/QEL17299

Low-threshold, single-transverse-mode, 940-nm vertical-cavity surface-emitting laser with a mode filter and half-wavelength cavity

Q.H. Ren, J. Wang, M. Yang, H.J. Wang, Z. Cheng, Y.Q. Huang, X.M. Ren, H.M. Ji, S. Luo

Abstract. **We demonstrate a structure for a vertical-cavity surface-emitting laser (VCSEL) with a mode filter and half-wavelength ($\lambda/2$) cavity. The effects of $\lambda/2$- and λ-cavities on the threshold current are studied. The thickness and etched diameter of the mode filter are optimised to achieve single-transverse-mode output. The results show that when changing from λ-cavity to $\lambda/2$-cavity, the threshold current of the VCSEL decreases by 30.7 % (from 0.85 mA to 0.65 mA). In addition, for the mode-filter thickness of 80 nm, and the etched diameter of 2.5 μm, the side mode suppression ratio reaches 90 dB, which meets the requirement of single-transverse-mode output. The VCSELs with the optimised design can overcome many difficulties and have great potential in 3D face recognition.**

Keywords: *VCSELs, mode filter, single-transverse-mode, half-wavelength cavity, threshold current.*

1. Introduction

Vertical-cavity surface-emitting lasers (VCSELs) are widely used in optical communications, optical interconnects, and optical information processing due to their low power consumption, effective coupling to fiber, low threshold current, and high power conversion efficiency [1, 2]. At present, the vast majority of VCSELs are employed in the field of electronic consumption, including proximity sensing in mobile phones, scanning of objects within a few meters, and laser radar systems in the autonomous driving that can detect obstacles more than 100 metres ahead [3–6].

In recent years, with the progress of research on VCSELs, the optical power, modulation bandwidth and reliability of VCSELs have been continuously improved. However, the application in optical communications is limited due to multi-transverse modes of VCSELs [7]. Therefore, it is vital to improve the single-transverse-mode output characteristics of VCSELs. So far, various methods have been proposed to realise single-transverse-mode output, such as, photonic crystal structure, small oxide aperture structure and mode filter structure [8–13]. In 2013, Tan et al. [14] realised a VCSEL with single-transverse-mode emission through a photonic crystal structure and demonstrated 25 Gb s^{-1} error-free transmission through a 1-km-long multimode fibre cable OM4 at a current density of 5.4 kA cm^{-2}. However, due to the complexity of photonic crystal it is difficult to realise this approach in experiments. In the same year, Safaisini et al. [15] realised a single-transverse-mode VCSEL with an oxide aperture of 3 μm. Unfortunately, as the oxide-confined aperture becomes smaller, the differential resistance, current density and internal temperature of the VCSEL inevitably increase. To solve these problems, in 2015, Larsson et al. [16] used a mode filter structure to achieve single-transverse-mode transmission. Previous research on single-transverse-mode VCSELs using a mode filter are mainly focused on the field of optical communications. However, there are only a few studies on single-transverse-mode VCSELs in the field of consumer electronics. With the increasing application of 940 nm VCSELs in mobile devices, eye safety and the stability of 3D recognition have attracted extensive attention and need to be improved urgently [17–19].

In addition, in order to reduce the power consumption in practical applications, the threshold current of the VCSEL is also the focus of attention. At present, there are three main methods for reducing the threshold current, including a small-sized oxide aperture structure, a photonic crystal structure, and a strain-compensated quantum well structure [20, 21]. In 2011, Lott et al. [22] designed an oxide aperture of 3 μm to achieve an 850 nm VCSEL output with a threshold current below 0.5 mA. In 2012, by using a photonic crystal structure, Xie et al. [23] successfully prepared an 850 nm VCSEL with a threshold current of 0.9 mA. In 2019, Yu et al. [24] finally realised a 940 nm VCSEL with the threshold current and slope efficiency of 0.95 mA and 0.96 W A^{-1}, respectively, using the gain characteristics of InGaAs/GaAsP strain-compensated quantum wells. Moreover, Mutig et al. [25] calculated the optical confinement factor of the VCSEL with a $\lambda/2$-cavity, equal to 5.1 %, which is 70 % larger than that of the VCSEL with a $3\lambda/2$-cavity. In theory, we know that the threshold current can be reduced by increasing the optical confinement factor, so it seems feasible to reduce the threshold current by shortening the cavity length [25].

Although many characteristics of VCSELs have been greatly improved, there are still some problems in the application of portable devices (mobile devices, wearable devices, notebook computers) [26, 27]. Thus, a 940 nm VCSEL with a $\lambda/2$-cavity and mode-filter structure has been proposed to solve these problems. By using a $\lambda/2$-cavity, the threshold current and energy consumption can be effectively reduced, and the service life can be extended as well. The mode-filter structure can control the optical mode output, and its output

Q.H. Ren, J. Wang, M. Yang, H.J. Wang, Z. Cheng, Y.Q. Huang, X.M. Ren State Key Laboratory of Information Photonics and Optical Communications, Beijing University of Posts and Telecommunications, Beijing 100876, China; e-mail: wangjun12@bupt.edu.cn;
H.M. Ji, S. Luo Center of Materials Science and Optoelectronics Engineering, University of Chinese Academy of Sciences, Beijing 100049, China

Received 25 February 2020; revision received 13 May 2020
Kvantovaya Elektronika **50** (8) 714–719 (2020)
Submitted in English

power can be very small, and the damage to the human eyes is negligible. Up to date, there have been few reports on the theoretical design and optimisation of 940-nm VCSELs used for 3D recognition, which require a low threshold and single-transverse-mode.

In this paper, we proposed a 940-nm VCSEL with a $\lambda/2$-cavity length and mode-filter structure. The threshold currents of the VCSELs with $\lambda/2$- and λ-cavities are investigated. The optical field distribution of the VCSELs is calculated by three-dimensional finite-difference time-domain method. The thickness and etched diameter of the mode filter are optimised to achieve a single-transverse-mode output. In addition, we analyzed the reasons for the threshold current reduction from the perspective of the optical confinement factor as well. The results show that compared with the traditional VCSELs, the optimised VCSEL has a lower threshold current and a higher output power. The threshold current is reduced from 0.85 mA to 0.65 mA, that is by 30.7%. The output power rose from 1.25 mW to 1.4 mW, with an increase of 10.7%. The thickness and etched diameter of the optimised mode filter are 80 nm and 2.5 μm, respectively. The side mode suppression ratio reaches 90 dB, which enables single-transverse-mode output. The optimised VCSEL is more suitable for practical application. Furthermore, it will promote the development of 940 nm VCSELs in the field of consumer electronics for near-infrared light sources in 3D recognition.

2. Device structure

The device structure of the VCSEL is illustrated in Fig. 1. The n-type (doping, 2×10^{18} cm^{-3}) mirror containing 34 pairs of $Al_{0.9}Ga_{0.1}As$/GaAs layers is designed as the bottom distributed-Bragg-reflector (DBR). The active region is composed of three pairs of $In_{0.11}Ga_{0.89}As$ (8 nm)/$Al_{0.2}Ga_{0.8}As$ (8 nm) quantum wells, sandwiched between two 51-nm cladding layers (from $Al_{0.2}Ga_{0.8}As$ to $Al_{0.9}Ga_{0.1}As$). The upper DBR mirror with 22.5 pairs of p-type (doping, 4×10^{18} cm^{-3}) $Al_{0.9}Ga_{0.1}As$/GaAs layers was grown on the active region. The cavity length is designed to be $\lambda/2$ [28]. In detail, for the first pair of the upper DBR on the active region, it is a 66.4-nm GaAs high-index layer with the optical thickness of $\lambda/4$. In sequence, there is a 47.8-nm $Al_{0.9}Ga_{0.1}As$ layer and a 30-nm $Al_{0.98}Ga_{0.02}As$ layer consisting of a low-index layer with the optical thickness of $\lambda/4$. A separate $Al_{0.98}Ga_{0.02}As$ layer is used to form a 6-μm aperture to confine the current and optical field, and effectively reduce diffraction loss. In addition, a GaAs layer is added between the p-type DBR and the ohmic contact layer for post-production of the mode-filter structure. Compared to unoxidised regions, the effective index of the oxidised region is reduced. Therefore, the oxidation-limited VCSEL structure can be regarded as a fibre model [29].

In this work, the optical field distribution and reflectivity of the VCSEL are simulated by the finite-difference time-domain method. The boundary condition is a perfectly matched layer. The thermal effects of the VCSEL are considered when analysing the photoelectric characteristics, including the Joule heat generated by differential resistance around the oxide layer, the absorption heat in doped semiconductor material in the DBRs, and nonradiative recombination heat generated by electrons and holes in the active region. The coefficients referenced from literature [29] are as follows: the internal optical loss is 10 cm^{-1}; the spontaneous emission coefficient is 2×10^{10} cm^3 s^{-1}; and the nonradiative and Auger recombination coefficients are 1×10^8 s^{-1} and 1.5×10^{-29} cm^6 s^{-1}, respectively. Other parameters of the materials used in the simulation are listed in Table 1.

3. Results and discussion

To optimise the VCSEL performance, we investigated the relationship between its photoelectric properties and material structure. The threshold current of the VCSEL with $\lambda/2$- and λ-cavities are compared, and then the thickness and etched diameter of the GaAs layer are optimised to form the mode filter.

Figure 2 shows the relationship between the output power and the threshold current. For a cavity length of $\lambda/2$, the threshold current is 0.65 mA, and the output power reaches a

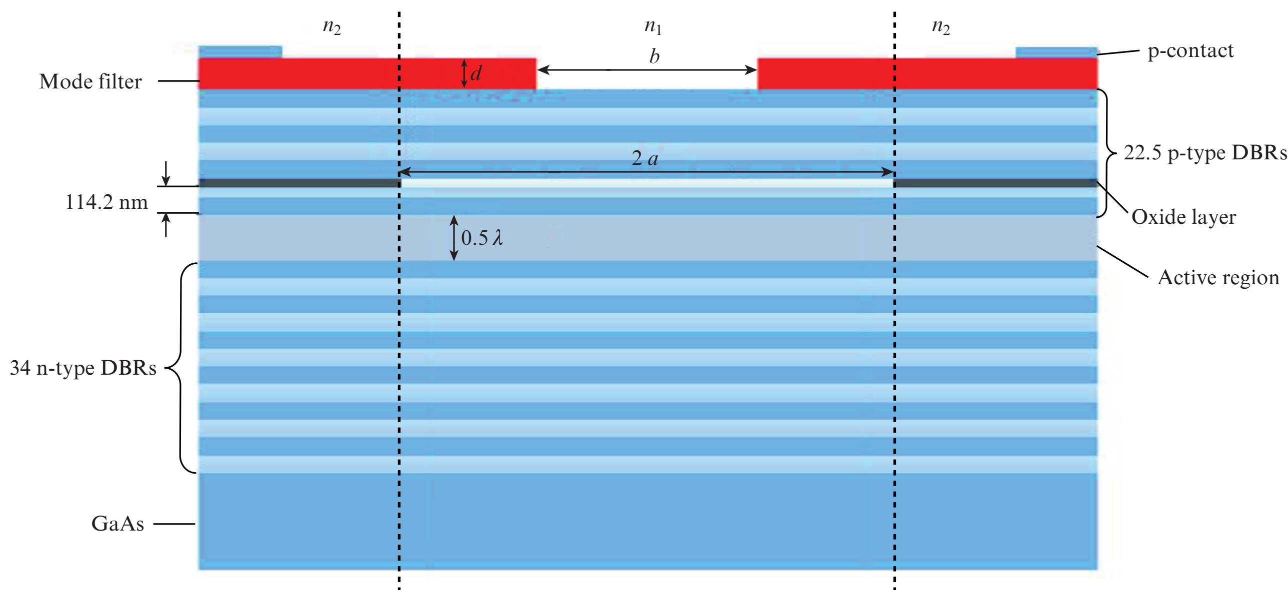

Figure 1. VCSEL structure: d and b are the thickness and diameter of the etched region of the mode filter; n_1 and n_2 are the effective refractive indices of the core region and the cladding region, respectively.

Table 1.

Material	Refractive index	Band gap/eV	Electron mobility/cm^2 V^{-1} s^{-1}	Conduction band density of states/10^{19} cm^{-3}	Valence band density of states /10^{19} cm^{-3}
$In_{0.11}Ga_{0.89}As$	3.56	1.210	10000	0.034	0.870
GaAs	3.54	1.424	8000	0.040	0.910
$Al_{0.2}Ga_{0.8}As$	3.42	1.673	4000	0.056	1.048
$Al_{0.9}Ga_{0.1}As$	3.04	2.128	205	1.540	1.575
$Al_{0.98}Ga_{0.02}As$	3.02	2.160	190	1.504	1.640

maximum of 1.4 mW at 6 mA. For a λ-cavity, the threshold current is 0.85 mA, and the output power reaches a maximum of 1.25 mW at a current of 5.5 mA. Thus, a VCSEL with a $\lambda/2$-cavity can reduce the threshold current by 30.8% compared to that with a λ-cavity.

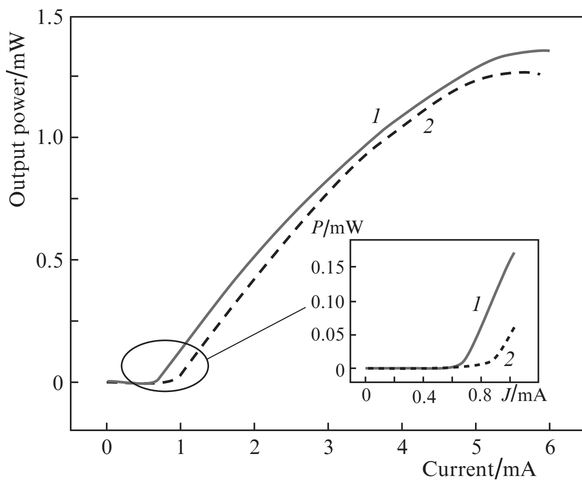

Figure 2. Output power vs. current for the VCSEL with (*1*) $\lambda/2$- and (*2*) λ-cavities.

In addition, the optical confinement factor of the both VCSELs is compared to further understand the above results [30, 31]. Figure 3a demonstrates the refractive index and the simulated optical field distribution in the traditional VCSEL with a λ-cavity. In the active region, the optical intensity peak in the centre is lower than that on both sides. Figure 3b shows the case of the VCSEL with $\lambda/2$-cavity. One can see that the optical intensity peak in the centre is higher than that on both sides; therefore, the optical field distribution is more advantageous for the $\lambda/2$-cavity, because the optical intensity peak in the centre is much stronger than that for the λ-cavity. Consequently, the overlap of the lasing mode with the active region increases, leading to a strong increase in the optical confinement factor. The optical confinement factor for the VCSEL with the $\lambda/2$-cavity is 3.44%, which is 12.5% lager than the value of the confinement factor for VCSELs based on the λ-cavity, where it is only 3%. The results show that in the VCSEL with a $\lambda/2$-cavity the optical confinement factor is higher and the threshold current is lower than those in the VCSE with a λ-cavity.

Second, we optimised the thickness d and etched diameter b of the GaAs layer, and obtained the optimal size to form the mode filter. For our further research, the number of transverse modes is calculated when the diameter of the oxide aperture is $2a = 6$ μm. Then, the dependence of the reflectivity of the transverse mode in the p-type DBR on the thickness d and the etched diameter b of the GaAs layer is investigated.

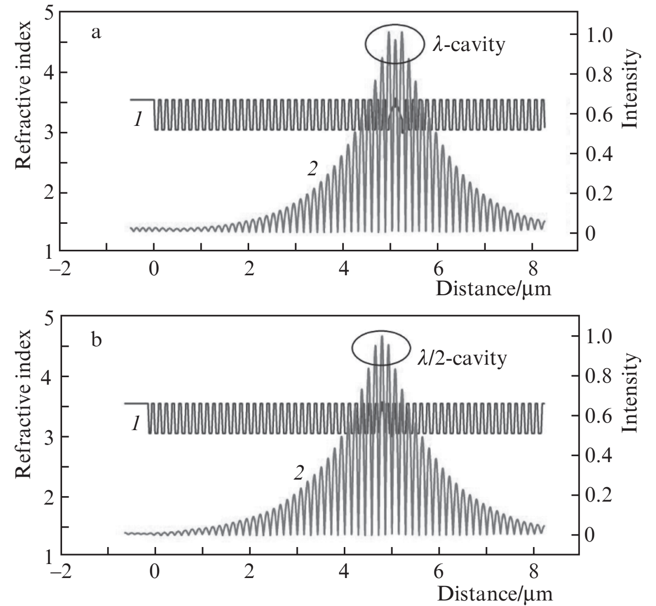

Figure 3. (*1*) Refractive index and (*2*) normalised optical field intensity of the VCSEL with (a) λ and (b) $\lambda/2$-cavities.

According to the fibre model theory, the normalised frequency V of the VCSEL can be written in the form

$$V = k_0 a\sqrt{n_1^2 - n_2^2}\,, \tag{1}$$

where k_0 is the vacuum wave vector [29]. The normalised frequency is the characteristic frequency of the LP_{mn} mode in the optical waveguide [29]. At $k_0 = 2\pi/\lambda$ ($\lambda = 940$ nm), $a = 3$ μm, $n_1 = 3.310$, and $n_2 = 3.303$, V is calculated to be 4.31. According to the relationship between the characteristic frequency and the number of LPmn modes, we conclude that there are four transverse modes, LP_{01}, LP_{11}, LP_{21} and LP_{02} in the cavity of the VCSEL, as shown in Figs 4a–4d.

The mechanism of the mode filter is to increase the difference of the reflectivity between the fundamental transverse mode and the higher-order transverse mode in the p-type DBR to achieve the mode selection. Thus, we need to optimise the thickness of the GaAs layer to minimise the reflectivity of the four transverse modes, and then etch the GaAs layer in the distribution region of the LP_{01} mode to form the mode filter [17]. In this case, the LP_{01} mode first reaches the emission condition due to the high reflectivity, while the other three high-order transverse modes cannot be emitted due to lower reflectivity (higher threshold current) under the same condition.

Figure 5a shows the relationship between the reflectivities of the four transverse modes and the thickness of the GaAs layer. As the thickness of the GaAs layer increases from 10 nm to 160 nm, the reflectivity of each transverse mode

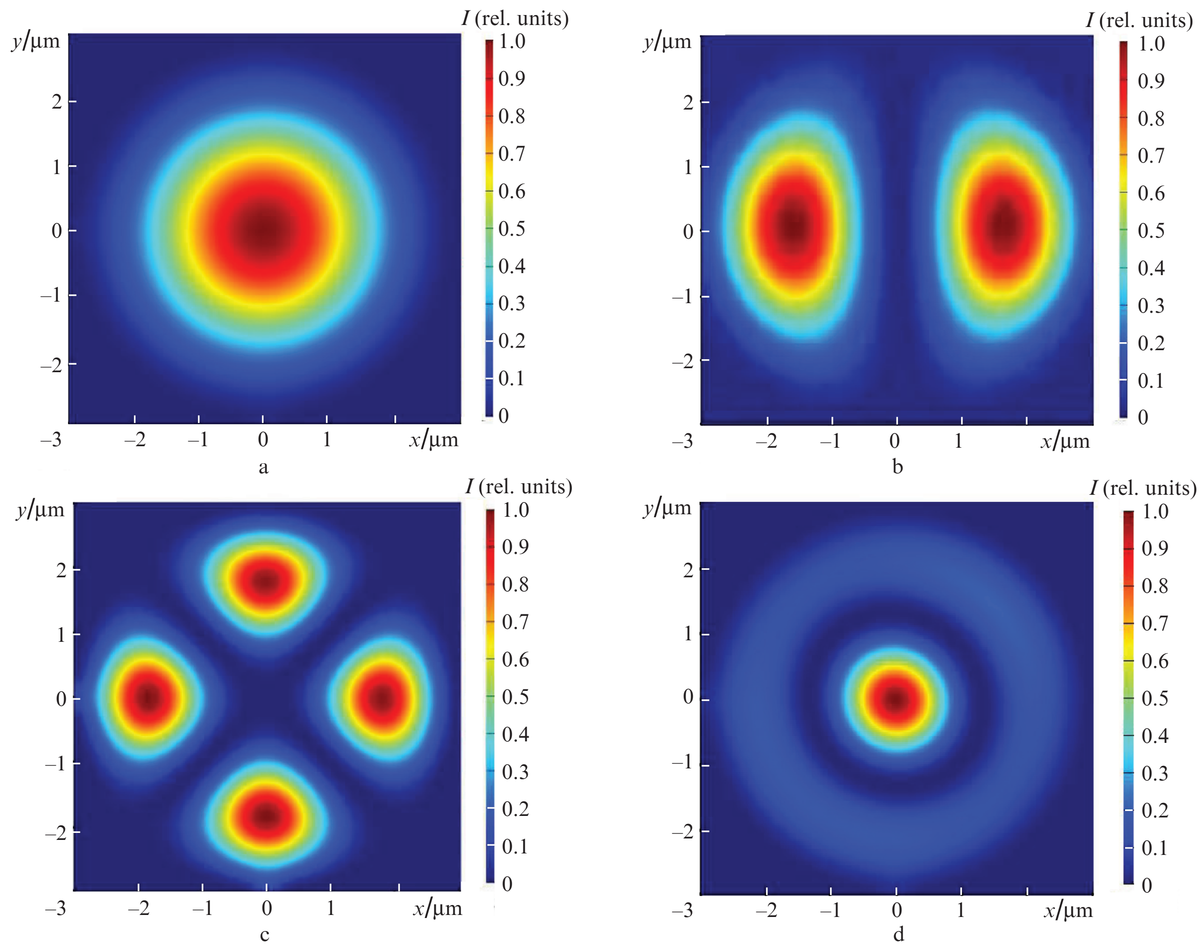

Figure 4. (Colour online) Distribution of modes with an oxide aperture of 6 µm: (a) LP_{01}, (b) LP_{11}, (c) LP_{21}, and (d) LP_{02}.

decreases firstly, and reaches a minimum at about 80 nm, then increases rapidly. According to the results, the thickness d of the mode filter is chosen to be 80 nm.

Figure 5b shows the relationship between the reflectivities of the four transverse modes and the etched diameter of the GaAs layer. By increasing the etched diameter of the GaAs layer from 0.5 to 5.5 µm, the reflectivities of the four transverse modes increase gradually, but the curves are not consistent. The reason is that the four transverse modes are differently distributed in the VCSEL cavity, and so the effect of the mode filter on the reflectivities of the four transverse modes is different at a same etched diameter.

In order to make the mode filter only suppress the higher-order transverse modes, the overlapping area (centre area) of the GaAs layer and the fundamental transverse mode must be etched away, with the other areas remaining without any changes. Therefore, we need to obtain an optimal etched diameter for the mode filter to maximize the difference of the reflectivities between the fundamental transverse mode and the three higher-order transverse modes. In this case, LP_{01} first reaches the emission condition, while the other three high-order transverse modes cannot be generated because of their lower reflectivities [32].

The difference of the reflectivities between the fundamental transverse mode and the three higher-order transverse modes as a function of the etched diameter of GaAs layer is plotted in Fig. 6. When the etched diameter of the GaAs layer is less than 2.5 µm, the difference of the reflectivities between LP_{01} and LP_{11}, LP_{21} increases. After the etched diameter exceeds 2.5 µm, the difference of the reflectivities tends to decrease, and the maximum value is obtained at 2.5 µm, which is 0.14% and 0.21%, respectively. The difference of the reflectivity between LP_{01} and LP_{02} reaches a maximum of 0.31% at the etched diameter of 3.5 µm. We also simulated the emission spectrum of the VCSEL, and obtained the side mode suppression ratio of 90 dB, which meets the requirements of the single-transverse-mode output. After comprehensive consideration, the etched diameter b of the mode filter is chosen to be 2.5 µm [32].

4. Conclusions

We have investigated a 940-nm VCSEL with $\lambda/2$-cavity length and mode-filter structure. The cavity length of the VCSEL is designed to be $\lambda/2$, which increases the optical confinement factor by 12.5% (from 3.01% to 3.44%) and reduces the threshold current reduces by 30.8% (from 0.85 mA to 0.65 mA). Then, the GaAs layer is added on the p-type DBR as a mode filter to control the single-transverse-mode output. The optimal thickness and etched diameter of the mode filter are obtained to be 80 nm and 2.5 µm, respectively. In addition, the side-mode suppression ratio reaches 90 dB, which meets the requirement of the single-transverse-mode output. We believe that our theoretical investigation and structure optimisation can provide solutions for fabricating high-quality VCSELs based on 3D recognition, and it will potentially improve the development of 940-nm VCSELs in the field of consumer electronics.

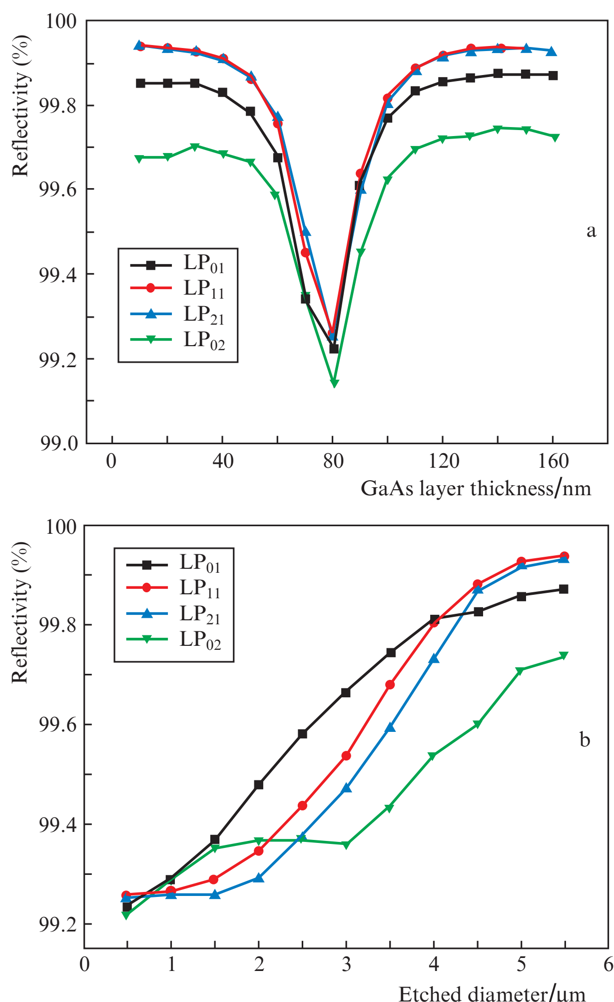

Figure 5. Dependences of the reflectivity on (a) the GaAs layer thickness and (b) etched diameter for different transverse modes.

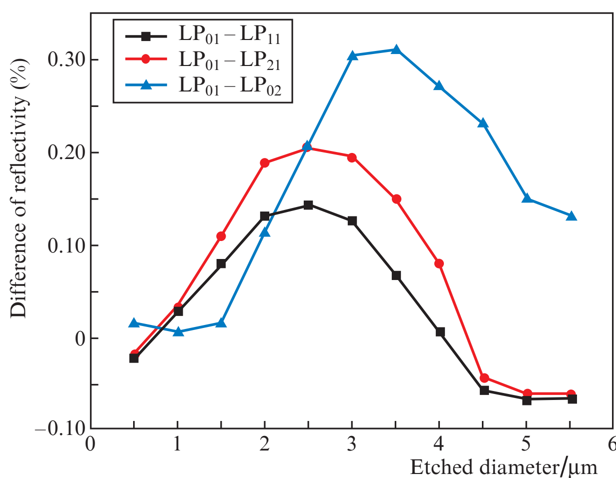

Figure 6. Difference of the reflectivity of modes vs. etched diameter.

Acknowledgements. This work was supported by the Natural National Science Foundation of China (NSFC) (Grant Nos 61874148, 61974141 and 61674020); Beijing Natural Science Foundation (Grant No. 4192043); National Key Research and Development Programme of China (Grant No. 2018YFB2200104); Beijing Municipal Science & Technology Commission (Grant No. Z191100004819012); State Key Laboratory of Information Photonics and Optical Communications, Beijing University of Posts and Telecommunications (Grant No. IPOC2018ZT01); and Project 111 of China (Grant No. B07005).

References

1. Shi J.-W., Wei C.-C., Chen J., Ledentsov N.N., Yang Y.-J. *Proc. SPIE*, **10122**, 101220F (2017).
2. Ledentsov N. Jr, Chorchos L., Turkiewicz J.P. *Proc. SPIE*, **10325**, 103250M (2017).
3. Moench H., Carpaij M., Gerlach P., Gronenborn S., Gudde R., Hellmig J., Kolb J., Lee A. *Proc. SPIE*, **9766**, 97660A (2016).
4. Warren M.E., Podva D., Dacha P., Block M.K., Helms C.J., Maynard J., Carson R.F. *Proc. SPIE*, **10552**, 105520E (2018).
5. Kondo T., Takeda K., Otama H., Murakami A., Sakurai J., Nakayama H., Gu X.-D., Koyama F. *Proc. SPIE*, **9766**, 97660C (2016).
6. Kondo T., Hayakawa J., Jogan N., Murakami A., Sakurai J., Gu X.-D., Koyama F. *Proc. SPIE*, **10122**, 1012203 (2017).
7. Liu A.-J., Wolf P., Lott J.A., Bimberg D. *Photon. Res.*, **7**, 121 (2019).
8. Yen J.-L., Chi K.-L., Jiang J.-W., Yang Y.-J., Shi J.-W. *IEEE J. Quantum Electron.*, **50**, 787 (2014).
9. Shchukin V., Ledentsov N.N., Kropp J., Steinle G., Ledentsov N. Jr, Burger S., Schmidt F. *IEEE J. Quantum Electron.*, **50**, 990 (2014).
10. Shi J.-W., Chen C.-C., Wu Y.-S., Goul S.-H., Kuo C., Yang Y.-J. *IEEE Photon. Technol. Lett.*, **20**, 1121 (2008).
11. Kao H.-Y., Tsai C.-T., Leong S.-F., Peng C.-Y., Chi Y.-C., Wang H.-Y., Kuo H.-C., Wu C.-H., Cheng W.-H., Lin G.-R. *Photon. Res.*, **6**, 666 (2018).
12. Kao H.-Y., Tsai C.-T., Leong S.-F., Peng C.-Y., Chi Y.-C., Huang J.-J., Kuo H.-C., Shih T.-T., Jou J.-J., Cheng W.-H., Wu C.-H., Lin G.-R. *Opt. Express*, **25**, 16347 (2017).
13. Shi J.-W., Yan J.-C., Wun J.-M., Chen J., Yang Y.-J. *IEEE J. Sel. Top. Quantum Electron.*, **19**, 7900208 (2013).
14. Tan M.P., Kasten A.M., Sulkin J.D., Choquette K.D. *IEEE J. Sel. Top. Quantum Electron.*, **19**, 4900107 (2013).
15. Safaisini R., Szczerba K., Westbergh P., Haglund E., Kogel B., Gustavsson J.S., Karlsson M., Andrekson P., Larsson A. *J. Opt. Commun. Netw.*, **5**, 686 (2013).
16. Larsson A., Westbergh P., Gustavsson J.S., Haglund E., Haglund E.P. *Proc. SPIE*, **9381**, 93810D (2015).
17. Safaisini R., Haglund E., Westbergh P., Gustavsson J.S., Larsson A. *Electron. Lett.*, **50**, 40 (2014).
18. Haglund E., Jahed M., Gustavsson J.S., Larsson A., Goyvaerts J., Baets R., Roelkens G., Rensing M., O'Brien P. *Opt. Express*, **27**, 18892 (2019).
19. Haglund A., Gustavsson J.S., Vukusic J., Modh P., Larsson A. *IEEE Photon. Technol. Lett.*, **16**, 368 (2004).
20. Shi J.-W., Yan J.-C., Wun J.-M., Chen J., Yang Y.-J. *IEEE J. Sel. Top. Quantum Electron.*, **19**, 7900208 (2013).
21. Feng M., Wu C.-H., Holonyak N. Jr. *IEEE J. Quantum Electron.*, **54**, 2400115 (2018).
22. Lott J.A., Payusov A.S., Blokhin S.A., Moser P., Ledentsov N.N., Bimberg D. *Phys. Status Solidi C*, **9**, 290 (2011).
23. Xie Y.-Y., Xu C., Kan Q., Wang C.-X., Chen H.-D., Shen G.-D. *Proc. Opt. Fiber Commun. Conf.* (Los Angeles, CA, 2012) p. 1.
24. Yu H.-Y., Yao S., Zhang H.-M., Wang Q., Zhang Y., Zhou G.-Z., Lü Z.-C., Cheng L.-W., Lang L.-G., Xia Y., Zhou T.-B., Kang L.-H., Wang Z.-Y., Dong G.-L. *Acta Phys. Sin.*, **68**, 064207 (2019).
25. Mutig A., Bimberg D. *Adv. Opt. Technol.*, **2011**, 1 (2011).
26. Cheng C.-H., Shen C.-C., Kao H.-Y., Hsieh D.-H., Wang H.-Y., Yeh Y.-W., Lu Y.-T., Huang Chen S.-W., Tsai C.-T., Chi Y.-C., Kao T.-S., Wu C.-H., Kuo H.-C., Lee P.-T., Lin G.-R. *Opto-Electron. Adv.*, **1**, 180005 (2018).
27. Park B., Keh Y., Lee D., Kim Y., Kim S., Sung K., Lee J. *IEEE Int. Conf. Computer Vision Workshop* (OSA, 2017) pp 2392 – 2398.
28. Hofmann W., Wolf P., Moser P., Larisch G., Unrau W., Mutig A., Kroh M., Bimberg D. *Proc. 23nd IEEE Int. Semiconductor Laser Conf.* (San Diego, CA, USA, 2012) pp 161 – 162.

29. Michalzik R. (Ed.) *VCSELs Fundamentals, Technology and Applications of Vertical-Cavity Surface-Emitting Lasers* (New York: Springer, 2013).
30. Corzine S.W., Geels R.S., Scott J.W., Yan R.-H., Coldren L.A. *IEEE J. Quantum Electron.*, **25**, 1513 (1989).
31. Kao H.-Y., Chi Y.-C., Tsai C.-T., Leong S.-F., Peng C.-Y., Wang H.-Y., Huang J.J., Jou J.-J., Shih T.-T., Kuo H.-C., Cheng W.-H., Wu C.-H., Lin G.-R. *Photon. Res.*, **5**, 507 (2017).
32. Wang X., Hao Y.-Q., Wang Z.-W., Xie J.-L., Zou Y.-G., Feng Y., Ma X.-H. *Proc. SPIE*, **10457**, 104571C (2017).